AD_____

Award Number: DAMD17-01-1-0811

TITLE: Noninvasive Detection of Microdamage in Bone

PRINCIPAL INVESTIGATOR: Dale R. Sumner, Ph.D.

CONTRACTING ORGANIZATION: Rush-Presbyterian-St. Luke's Medical Center
Chicago, Illinois 60612

REPORT DATE: October 2003

TYPE OF REPORT: Final

PREPARED FOR: U.S. Army Medical Research and Materiel Command
Fort Detrick, Maryland 21702-5012

DISTRIBUTION STATEMENT: Approved for Public Release;
Distribution Unlimited

The views, opinions and/or findings contained in this report are those of the author(s) and should not be construed as an official Department of the Army position, policy or decision unless so designated by other documentation.

REPORT DOCUMENTATION PAGE

Form Approved
OMB No. 074-0188

1. AGENCY USE ONLY (Leave blank)	2. REPORT DATE	3. REPORT TYPE AND DATES COVERED
	October 2003	Final (10 Sep 01-10 Sep 03)

4. TITLE AND SUBTITLE

Noninvasive Detection of Microdamage in Bone

5. FUNDING NUMBERS

DAMD17-01-1-0811

6. AUTHOR(S)

Dale R. Sumner, Ph.D.

7. PERFORMING ORGANIZATION NAME(S) AND ADDRESS(ES)

Rush-Presbyterian-St. Luke's Medical Center
Chicago, Illinois 60612

E-Mail: Rick_Sumner@rush.edu

8. PERFORMING ORGANIZATION REPORT NUMBER

9. SPONSORING / MONITORING AGENCY NAME(S) AND ADDRESS(ES)

U.S. Army Medical Research and Materiel Command
Fort Detrick, Maryland 21702-5012

10. SPONSORING / MONITORING AGENCY REPORT NUMBER

11. SUPPLEMENTARY NOTES

12a. DISTRIBUTION / AVAILABILITY STATEMENT

Approved for Public Release; Distribution Unlimited

12b. DISTRIBUTION CODE

13. ABSTRACT (Maximum 200 Words)

This concept exploration proposal seeks to determine if a novel x-ray technique called diffraction enhanced imaging, which provides dramatic gains in contrast over conventional radiography, can be used to identify microdamage in bone non-invasively. This technique has been used successfully in soft tissues, including recent studies by our group to detect damage in articular cartilage. Here, we plan to extend our work to studies relevant to microdamage accumulation and repair in bone. Interest in microdamage in bone comes in part from its likely role in the etiology of stress fractures. In addition, microdamage accumulation may contribute to osteoporotic fractures and loosening of dental or orthopedic implants. Our working hypothesis is that microdamage in bone can be detected non-invasively by diffraction enhanced imaging because this imaging modality expands the ability of x-rays to record refraction and scatter rejection (extinction) as well as absorption. No matter the spatial scale of the fracture feature, diffraction enhanced imaging has a contrast mechanism suited to make the feature visible. We outlined two specific aims, with initiation of specific aim 2 dependent upon successful completion of specific aim 1. Although there were some positive indications in a series of six experiments, it is not yet clear that microdamage can be detected by DEI. Our conclusion is that a number of technical limitations, especially the resolution of the detector, inhibited our ability to give the hypothesis the best test.

14. SUBJECT TERMS

microdamage, bone, diffraction enhanced imaging, synchrotron, fatigue fracture, non-invasive

15. NUMBER OF PAGES

34

16. PRICE CODE

17. SECURITY CLASSIFICATION OF REPORT	18. SECURITY CLASSIFICATION OF THIS PAGE	19. SECURITY CLASSIFICATION OF ABSTRACT	20. LIMITATION OF ABSTRACT
Unclassified	Unclassified	Unclassified	Unlimited

Table of Contents

***Revised sections of the original final progress report**

INTRODUCTION

This concept exploration proposal seeks to determine if a novel x-ray technique called diffraction enhanced imaging, which provides dramatic gains in contrast over conventional radiography, can be used to identify microdamage in bone non-invasively. This technique has been used successfully in soft tissues, including recent studies by our group to detect damage in articular cartilage. Here, we plan to extend our work to studies relevant to microdamage accumulation and repair in bone. Interest in microdamage in bone comes in part from its likely role in the etiology of stress fractures. In addition, microdamage accumulation may contribute to osteoporotic fractures and loosening of dental or orthopedic implants. Our working hypothesis is that microdamage in bone can be detected non-invasively by diffraction enhanced imaging because this imaging modality expands the ability of x-rays to record refraction and scatter rejection (extinction) as well as absorption. No matter the spatial scale of the fracture feature, diffraction enhanced imaging has a contrast mechanism suited to make the feature visible. Specific studies to determine the optimum imaging parameters and to compare diffraction enhanced images of machined samples and intact bones before and after induction of mechanical testing have been designed to address the hypothesis.

This is a revised final report. It includes all of the original final report. In addition, we have added three draft manuscripts in the Appendix:

- Identification of Fatigue Damage in Cortical Bone by Diffraction Enhanced Imaging
- Diffraction Enhanced Imaging of Controlled Defects within Cortical Bone, Including Bone-Implant Interface Gaps
- Three-dimensional Diffraction Enhanced Imaging

We also provide a point-by-point response to the review of the original final report (dated December 2003) here.

"...the work is not in compliance with the original Statement of Work ...a better explanation of why the goals were not met should have been included"

In the interim progress report we noted why there was a deviation from the Task 1. Essentially, we decided to follow the recommendation of the reviewers of the original grant application. The project, as originally conceived, was dependent upon successful completion of Task 2. As documented in the original final report and as now more clearly described in the draft manuscript ("Identification of Fatigue Damage in Cortical Bone by Diffraction Enhanced Imaging"), we encountered a number of technical difficulties. Some of these have been addressed, but others, especially the issue of spatial resolution, have not yet been solved. Indeed, a colleague and co-investigator on the DoD grant has submitted a Shared Instrumentation Grant to the NIH to acquire a new detector. The subsequent tasks do not merit attention until Task 2 is successfully addressed. To explore the capabilities of imaging bone with DEI, given the constraints made apparent by the experiments performed in addressing Task 2, we decided to put some effort into imaging problems that would not be adversely affected by the spatial resolution issues and that would test the capabilities of DEI. To that end, we performed the experiments now outlined in the second two draft manuscripts.

"It is not clear that the use of control specimens or ambient rocking curve measurements meet the requirements for quality control leading to clean measurements of fatigue properties."

We concur with this criticism and have more clearly delineated the current status in the first draft manuscript.

"The weakness of the report is the poor organization of the results."

"...this Final jReport should include a much better discussion of the overall findings ... allude to specific tables and figures..."

"...The report ... did not adhere to the standards of a scientific publication."

"Revision of the report to include a bolded or italicized discussion of the significance of each task is recommended."

We believe the draft manuscripts will address these concerns. In the original final report, we thought it important to detail our work experiment-by-experiment because of the numerous technical problems.

BODY

We have focused on Task 2 because it is the most important part of the proposed work. The reviewers of the grant felt that Task 1 was not important. In addition, we have modified the experimental design to accommodate the practicality of access to the key resource in the project -- the National Synchrotron Light Source (NSLS) at Brookehaven National Laboratory and have eliminated the need to subject the specimens to freeze-thaw cycles (Task 1).

Our working hypothesis for this concept exploration proposal was that microdamage in bone can be detected non-invasively by diffraction enhanced imaging (DEI) because of the inclusion of refraction and scatter rejection (extinction) contrast mechanisms in addition to absorption in this radiographic imaging modality. We outlined two specific aims, with initiation of specific aim 2 dependent upon successful completion of specific aim 1. Although there were some positive indications in a series of experiments, it is not yet clear that microdamage can be detected by DEI. Hence, we did not progress to specific aim 2. Our conclusion is that a number of technical limitations inhibited our ability to give the hypothesis the best test. Specifically, a limitation in the spatial resolution of the detector proved to be a more daunting challenge than originally anticipated. We believe that with better instrumentation (spatial resolution of the detector) that it would be possible to identify microdamage in bone definitively. In conducting these experiments we realized that DEI might be useful for other musculoskeletal imaging problems and did perform initial experiments on examination of the bone-implant interface and extending the technique to three-dimensional imaging (microCT-DEI).

The accompanying table summarizes the experiments performed. All experiments were geared toward testing Task 2 of specific aim 1.

Experiment	Date at NSLS	Imaging medium	Key Findings
1.2a	Jan '02	film	Detection of "large" (0.4-1.6 mm) defects (Oct '02 Prog report Fig. 1 with additional analyses reported here)
1.2b			Detection of non-displaced fracture (Oct '02 Prog report)
1.2c			Detection of microdamage (Oct '02 Prog report Fig 2) – width of rocking curve appeared greater for unstressed samples
1.2d (called 2a in Oct '02 Prog report)	Aug '02	Image plate	Detection of graded levels of microdamage (Oct '02 report only indicated experimental problems with graded damage induction, here we provide more information)
1.2e	Oct '02	CCD	Problems with CCD detector make interpretation of data difficult
1.2f	March '03	Image Plate CCD	Detection of microdamage by examining rocking curve width – 8 of 9 test samples have wider rocking curve widths after induction of microdamage by fatigue loading. However, the one control bone also had an increase in rocking curve width even though it was not fatigue loaded
1.2g	July '03	CCD	Detection of microdamage by examining rocking curve width – rocking curve width of fatigued bones decreased less than that for control bones
1.2h			Comparison of cortical and trabecular bone – no difference in rocking curve width
1.2i			Computed tomography imaging
1.2j	Oct '03	CCD	Change in rocking curve width over time – bones stored and imaged in fluid showed a slight increase in rock curve width between different imaging sessions, whereas bones stored in desiccator or open air had larger increases in rocking curve width between imaging sessions
1.2k			Bone-implant interface – analysis in progress
1.2l			Trabecular bone quality – analysis in progress
1.2m			Defect detection – analysis in progress

The grant was initiated in September of 2001 and the first available beam time at NSLS was in January of 2002. For experiments designed to examine microdamage (1.2c, 1.2d, 1.2e, 1.2f, 1.2g, and 1.2j), we used machined bovine cortical bone "matchstick" samples (roughly 4-5

mm in cross-section by 30 to 50 mm in length). These samples were imaged, fatigue loaded (except for the controls), and then re-imaged. In most experiments, the samples were loaded in three-point bending until there was approximately a 20% reduction in structural stiffness. During imaging, careful attention was paid to repositioning so that comparable regions of a given specimen could be examined before and after induction of damage by fatigue loading. The underlying concept was that this sort of paired experimental design would maximize the possibility of detecting microdamage. The main endpoint in these experiments was a calculation of the width of the rocking curve. We expected that the rocking curve width would be slightly widened after mechanical loading due to additional scattering caused by microfractures in the loaded bone.

Experiment 1.2a-c (January '02). Most of the data from the January 2002 experiments were described in the annual review (October '02 progress report). Since then, we have performed additional analyses relevant to Experiment 1.2a and found that DEI provides quantitatively higher intrinsic resolution of compact bone structure and simulated defects within the bone, suggesting that DEI is a promising method for detecting low-contrast lesions. Briefly, bovine cortical bone samples (5x5x50 mm) were prepared and had drill holes with diameters of 1/64" (0.4 mm), 1/32" (0.8 mm), 3/64" (1.2 mm) and 1/16" (1.6 mm). A monochromatic radiograph (obtained using a synchrotron) and DEI images (at three positions of the analyzer crystal) were taken at 30 keV using the X-15 beamline at the National Synchrotron Light Source, Brookhaven National Laboratory.

Figure 1(a), (b), and (c) are a radiograph, a DEI apparent-absorption image, and a DEI refraction image, respectively, of a bone specimen with four drill holes of increasing diameters. In all three images, each of the holes was visible, as were the vascular channels throughout the bone. However, the resolution and, therefore, the contrast of the DEI absorption and refraction images were greater than that of the radiograph. Specifically, the DEI absorption image was measured to have an effective point spread function (PSF) 125μm (2.5 pixels) narrower than that of the radiograph (in terms of full width at half-maximum (FWHM)). Since the absorption and refraction images describe different physical properties, further image comparison was performed by way of the normalized mutual information (NMI) between neighboring pixels. In essence, NMI quantifies similarity between neighboring pixels, where, all else being equal, smaller NMI indicates higher resolution. Note that this method of comparing image resolution is meaningful only for images, as in our studies, that have high signal-to-noise-ratio and similar radiation dose. NMI was measured to be 0.59, 0.27 and 0.21 for the radiograph, the DEI apparent absorption image, and the DEI refraction image, respectively. NMI identifies the DEI refraction image as the image with the highest spatial resolution. This agrees with visual inspection of Figure 1. In addition, because of the physics of DEI, the refraction image has an edge-enhancement property which is apparent in the vascular channels, drill-hole defects, and the

a b c

Figure 1. Images of bone: (a) radiograph; (b) DEI apparent absorption image; and (c) DEI refraction image.

lumens of the large vascular channels which are discernable within the DEI images.

In this analysis, we have shown that DEI provides significantly greater resolution of bone structure than conventional radiography. This is in part because the X-ray scatter that degrades the contrast of conventional radiography is removed in DEI. Additionally, because the refraction index is greatest at boundaries between different tissues and between tissue and spaces, DEI refraction images provide a significant edge enhancement and three-dimensional appearance at these borders. In summary, due to the ability of DEI to reject X-ray scatter and to harness X–ray refraction properties of tissues, it renders radiographs of bone tissue of extremely high contrast. Thus, DEI holds promise for the identification of bone lesions that are early in development, small, or have little contrast, and which are therefore difficult to identify with conventional radiography.

Experiment 1.2d (August '02). We used 5 bovine cortical bone match stick samples. All were imaged by DEI and then samples 2-5 were returned to Rush to induce fatigue damage. The goal was to have one sample with no fatigue damage (specimen 1) and four samples with 15% to 60% reduction in stiffness (a mechanical measurement of damage). The graded loading proved more difficult than anticipated and two specimens broke during mechanical loading. The remaining two specimens had approximately 20% reduction in stiffness. We anticipated that the rocking curve width would be slightly widened after mechanical loading due to additional scattering caused by microfractures in the loaded bone. Unexpectedly, three of the four samples showed a reduction in width (FWHM) of the rocking curve after the specimens were fatigue loaded (Table 1). The one sample which had an increased FWHM was one of the two samples which broke during the mechanical loading. Bone 1, which was not fatigue loaded, also showed a decrease in the width of the rocking curve. In fact, this decrease was greater than three of the loaded specimens so it is possible that relatively the loaded specimens did, in fact, have a slightly increase in rocking curve width.

Table 1 (Experiment 1.2d)

Bone	Group	Pre-Mechanical loading		Post-mechanical loading		Post - Pre
		Rocking curve width (FWHM)^	Standard deviation	Rocking curve width (FWHM)^	Standard deviation	
*1	Control	1.78	0.12	1.51	0.09	-0.27
2	Loaded	1.64	0.26	1.51	0.09	-0.13
**3	Loaded	2.35	0.23	1.88	0.14	-0.47
**4	Loaded	1.89	0.49	1.99	0.07	0.10
5	Loaded	1.75	0.25	1.54	0.08	-0.22

*not mechanically loaded between Pre and Post Rocking Curve Width determination
**broke during mechanical loading
^adjusted for ambient rocking curve width

Experiment 1.2e (October '02). As with the August 2002 experiment (Experiment 1.2d), the rocking curve FWHM's of 5 cortical bones were measured. Four bones were then shipped to Rush to be fatigue loaded, two of which broke in the fatigue loading process. The rocking curve FWHM's for the 3 unbroken bones and the 4 bone halves were then measured. For this set of data, all data were collected using a new CCD detector. Unfortunately, stability

issues were encountered with the new experimental setup. Measurements of the ambient rocking curve FWHM, which should not have fluctuated by more than a couple hundredths of a microradian between scans, varied over a range of 0.5 μradians. Because of the significant variations in the ambient measurements, the rocking curve FWHM's from this experiment were determined to be unreliable.

Experiment 1.2f (March '03). The goal of this experiment was to provide additional data on fatigue loading-induced change in the width of the rocking curve because the results from Experiment 1.2d were not entirely in agreement with the expected result that the rocking curve width would be absolutely widened due to additional scattering caused by microfractures in the loaded bone. In addition, to provide additional data on the reliability of the CCD, images were collected with both the image plate and the CCD. Adjustments to the CCD were made between Experiment 1.2e and the present experiment. A beam of 40 KeV x rays was incident on the sample holder which contained bovine cortical bones (machined to approximately 5mm by 5mm by 50 mm) that were immersed in distilled water. Fiducials were fixed to the sample holder to aid in the alignment of the rocking curve scans. The sample stage was moved so that the fixed beam from the source passed through the middle of the bone of interest. The analyzer crystal was scanned to ensure that the peak was set to the zero position. For the image plate, the analyzer crystal was then rocked from –5 □radians to +5 □radians. The image plate was exposed for 1 second at each of the 0.2 □radian steps on the scan then shifted up by 3.3mm for each subsequent scan. For the CCD, the analyzer crystal was rocked from -10 □radians to +10 □radians in 0.2 □radian steps. A separate frame was retrieved from the CCD for each scan (a total of 101 frames). The shutter was closed for frames 93 through 101 and the values of those frames were averaged together to find the background.

The rocking curve widths were obtained using IDL. For the image plate, the image was read into IDL and then each of the 51 steps of the scan was cut. For both the CCD and image plate, the median for each individual step of the scan was found in the y-, or vertical, direction. For each value in the x-direction the median y value for each step was fit to a gaussian and the full width at half of the maximum (FWHM) was found.

After mechanical loading, the rocking curve width was increased in 8 of the 9 mechanically loaded specimens, whether assessed with the image plate or the CCD (Table 2). Inexplicably, the rocking curve width of the one control bone also increased from the first to the second imaging session. In fact, the increase was roughly 3-fold greater than the average increase for the mechanically loaded specimens.

Table 2 (Experiment 1.2f)

		Image plate			CCD		
		Rocking Curve Width (FWHM)^			Rocking Curve Width (FWHM)^		
Specimen	Group	Pre	Post	Post - Pre	Pre	Post	Post - Pre
*1	Control	1.74	1.95	0.21	1.71	2.28	0.57
2	Loaded	0.9	1.03	0.13	0.82	0.99	0.17
3	Loaded	1.92	2.14	0.22	1.84	2.43	0.59
4	Loaded	1.08	1.14	0.06	1.02	1.2	0.18
5	Loaded	0.87	0.95	0.08	0.83	0.92	0.09
6	Loaded	1.26	1.36	0.1	1.3	1.4	0.1
7	Loaded	1.26	1.42	0.16	1.27	1.5	0.23

		Image plate			CCD		
		Rocking Curve Width (FWHM)^			Rocking Curve Width (FWHM)^		
Specimen	Group	Pre	Post	Post - Pre	Pre	Post	Post - Pre
8	Loaded	1.15	1.23	0.08	1.18	1.22	0.04
9	Loaded	1	1.06	0.06	0.99	1.11	0.12
10	Loaded	1.53	1.37	-0.16	1.53	1.45	-0.08
Average for loaded specimens				0.08			0.16

*not mechanically loaded between Pre and Post Rocking Curve Width determination
^adjusted for ambient rocking curve width

As stated previously, the goal of this experiment was to determine whether or not the rocking curve of loaded bovine cortical bone differed measurably and reproducibly from that of unloaded bone. A paired design was used in which each bone sample was imaged before and after loading. It is difficult to make a concrete statement about either the measurability or the reproducibility of the difference between pre- and post-loaded rocking curves because of the even larger change in the control bone. There are several possible explanations for the change in the control bone rocking curve. It is possible that the response of the detector was different for different intensities of the x-ray beam. However, because of the similar findings for the image plate and CCD, it is unlikely that the unexpected finding in the rocking curves of the control bone was due to differences in intensity response. Another possibility is that control bone tissue degraded between scans, but we believe this is unlikely because the same effect would be expected in the loaded samples. It appears that the most probable explanation for the change in the control bone's rocking curve measurements was drifting in either the monochromator or in the analyzer crystal. Drifting of either the monochromator or the analyzer could cause either a narrowing or a widening of the rocking curve. This raises the possibility, however, of similar drifts during data collection for the loaded specimens.

Part of this experiment was to determine if there was a measurable difference between the results that were obtained using the image plate and those obtained with the CCD. The data show that there is a consistency between the two. Stability issues with the CCD that were a problem in Experiment 1.2.e were resolved, so it was determined that the CCD could replace the image plate for future experiments.

Experiment 1.2g (July '03). After running into some unexplained changes in the rocking curve widths of control bones in the past, we decided to use several control bones as opposed to just using one bone. A total of 18 bovine cortical bone samples were prepared. As in the previous experiments, all samples were imaged at the NSLS, then shipped to Rush for fatigue loading of the test specimens, then shipped back to NSLS for a second imaging session. We took rocking curves of each of the bones in the horizontal position and the vertical position. The corrected horizontal rocking curve widths (in μradians) are included in Table 3.

Table 3 (Experiment 1.2g)

Control*				Loaded			
	Rocking Curve Width (FWHM)^				Rocking Curve Width (FWHM)^		
Specimen	Pre	Post	Post-Pre	Specimen	Pre	Post	Post-Pre
2	0.727	0.609	-0.12	1	0.996	0.912	-0.08
3	1.254	0.914	-0.34	10	0.880	0.755	-0.12

Control*				Loaded			
	Rocking Curve Width (FWHM)^				Rocking Curve Width (FWHM)^		
Specimen	Pre	Post	Post-Pre	Specimen	Pre	Post	Post-Pre
4	0.920	0.779	-0.14	11	1.097	0.803	-0.29
5	1.057	0.794	-0.26	12	1.221	0.981	-0.24
6	1.448	1.149	-0.30	13	0.744	0.681	-0.06
7	1.506	1.455	-0.05	14	1.128	1.068	-0.06
8	0.909	0.811	-0.10	**15	0.844		
9	1.846	1.579	-0.27	16	1.504	1.468	-0.04
				17	0.923	0.801	-0.12
				**18	0.999		
Average			-0.20				-0.13
standard deviation			0.11				0.09

*not mechanically loaded between Pre and Post Rocking Curve Width determination
**broke during mechanical loading
^adjusted for ambient rocking curve width

The corrected rocking curve widths of all the bones decreased between the first and second imaging sessions (i.e., pre and post mechanical loading). The decrease was greater on average for the control bones than for the stressed bones. Thus, in Experiment 1.2d, the rocking curve narrowed less in the loaded bones than in the one control and in Experiment 1.2g, the rocking curve narrowed less in the 8 loaded bones than in the 8 controls. Experiment 1.2f appears to be an outlier in that the rocking curve widened less in the loaded bones than in the one control bone.

Experiment 1.2h (July '03). Four bovine samples (two trabecular and two cortical), measuring approximately 4mm by 4mm by 40mm were imaged. Several rocking curve scans were done for each of the bones in the horizontal orientation. Unexpectedly, the rocking curve widths did not differ consistently between trabecular and cortical bone. As expected, the cortical bone attenuated about three times as much beam as the trabecular bone. Despite the lack of difference in rocking curve width, there were obvious differences in the images and it is known that the microscopic structure of cortical and trabecular bone is vastly different. In the future, the focus should be to determine what information can be derived from the images using other image analysis and processing tools in addition to the width of the rocking curve.

Experiment 1.2i (July '03). Several different computed tomography scans of two cylindrical samples of trabecular bovine bone were performed. For each analyzer crystal scan angle, 360 images were taken of the sample at one degree increments. The scan time for each analyzer crystal angle was approximately 15 minutes with a one second scan time for each sample angle. The analyzer crystal was set at +0.8μrads from the peak of the rocking curve, the corresponding negative side of the rocking curve, and the peak of the rocking curve. The monochromator and analyzer crystal were retuned between scans to minimize the crystal drift between scans. To date, we have completed only very rough initial processing using code for IDL that was obtained from http://www-fp.mcs.anl.gov/xray-cmt/rivers/tutorial.html. While

some artifacts remain, we are confident they can be removed with further processing. The images, even at this stage, are promising.

Figure 2

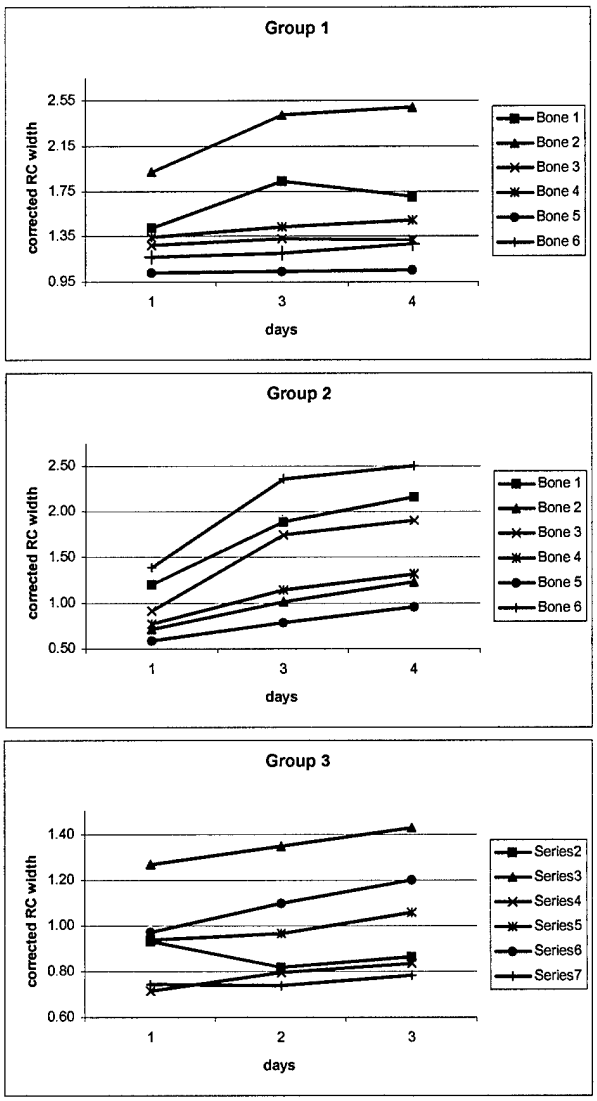

Experiments 1.2j-m (October '03). These experiments were performed just after the grant period ended. Here only Experiment 1.2j is described in detail because it is an important follow-up to previous experiments on the issue of change in rocking curve widths between imaging sessions. In previous experiments, we had found that the corrected rocking curve widths of control samples (stored in 10% formalin solution and imaged in water) changed (decreased or increased) by about 0.1 to 0.6 microradians over a time period of about 5 days. We hypothesized that the rocking curve changes were due to water seeping into or out of the cavities in the cortical bone. For this experiment, three groups of six bovine cortical bone match stick samples were imaged under 3 different conditions. All bones were received at the NSLS in 10% neutral buffered formalin on October 8, 2003 and imaged immediately. The bones in Group 1 were subsequently stored in a desiccator and imaged in air. Group 2 samples were subsequently stored in open air and imaged in water. Group 3 samples were subsequently stored in 10% formalin and imaged in water. Rocking curve images were taken on the date of receipt, 2 days later and then after one additional day.

The rocking curves for all groups increased from the first to the third imaging session (Fig. 2). The average increases (and standard deviations) from the first to the last imaging sessions were 0.20 (0.21), 0.75 (0.31), and 0.10 (0.10), for Groups 1, 2 and 3, respectively. Thus, because loss of water in the bone's pores (Groups 1 and 2) was associated with widening of the rocking curve, it is likely that previous findings of narrowing of the rocking curve (Experiments 1.2d and 1.2g) may have been caused by additional fluid seeping into the pores during the experiment. However, Group 3 also experienced a slight increase in the rocking curve width, which is somewhat inconsistent with Experiments 1.2d and 1.2g, but consistent with Experiment 1.2f. The magnitude of the increase was smaller in Group 3 than in either Group 1 or Group 2, and may represent "drift" during the course of the experiment that was not successfully corrected with the ambient rocking curve measurements.

Discussion: Challenges to making quantitative comparisons

There are technical and analysis challenges to making these quantitative comparisons. For instance, the medium used to collect the images must be considered and understanding the practicality of each method is important. By far, the best spatial resolution can be obtained when radiographic film is used. However, film processing is cumbersome at the NSLS, not always available and can severely limit the number of imaging sessions within a run because of the slow turn-around time. Accordingly, we collected data with an image plate and later with a charged couple device (CCD). The CCD is advantageous because of the rapid data acquisition and ease of handling digital data. The main limitation is the resolution (on the order of 50 μm). Microcracks in bone are on the order of 50 to 100 μm in length, but only 1 to 2 μm in width. We thought the spatial limitation could be overcome by searching for a "signature" in the images. Therefore, we turned to analysis of the width of the rocking curve, which should be informative about scatter rejection. However, it is now apparent that rocking curve width tends to drift over time, even when corrections are made for the ambient rocking curve. Thus, it is now apparent that rather large number of control specimens need to be processed simultaneously with experimental specimens. Even when this was done (Experiment 1.2g), the variability between specimens did not permit detection of the loading effect. In fact, given the magnitude of the difference between the control and loaded specimens and the variability, a sample size of 33 would have been needed to show a significant difference ($\alpha = 0.05$, $\beta = 0.80$). It may be possible to apply another image analysis technique (in addition to rocking curve width determination) to improve the ability to identify microdamage.

KEY RESEARCH ACCOMPLISHMENTS

- Confirmation that Diffraction Enhanced Imaging highlights surface (external and internal) features.
- It seems possible that microdamage can be detected by comparing the "rocking curve" widths of samples before and after induction of damage, but a better resolution camera will be needed to provide a more rigorous test.
- It may be possible that the other image analysis modalities can also be used to detect the presence of microdamage.

REPORTABLE OUTCOMES

1. Connor DJ, Sayers D, Lalush D, Sumner DR, Zhong Z: Diffraction enhanced computed tomography of trabecular bone. APS Conference, 2004
2. Connor DM, Sayers D, Kiss M, Zhong Z, Sumner DR: Rocking curve analysis of stressed and unstressed cortical bone. International Conference on Synchrotron Radiation Instrumentation, 2003

3. Sumner DR: Fixation of implants. *In: The adult knee,* ed by JJ Callaghan, AG Rosenberg, HE Rubash, PT Simonian and TA Wickiewicz., p 289. Philadelphia, Lippincott Williams & Wilkins, 2003.

- Personnel receiving support: D.R. Sumner (Rush), C. Muehleman (Rush), DJ Connor (North Carolina State University).

CONCLUSIONS

Although previous studies with DEI have demonstrated the ability of this modality to identify qualitative differences not recognizable otherwise (e.g., detection of cartilage damage), attempting quantitative analysis of the images places additional technical challenges that currently limit our ability to detect microdamage in bone. The basic physics principles, as outlined in the original grant, are still relevant and we recommend use of a better resolution camera and the application of other forms of analysis than rocking curve width determination.

REFERENCES

none

Identification of Fatigue Damage in Cortical Bone by Diffraction Enhanced Imaging

Statement of Problem

The purpose of this experiment was to determine if Diffraction Enhanced Imaging (DEI) could be used to detect microdamage that results from fatigue loading bovine cortical bone.

Background

Bone fracture

In order for fracture to occur in any material there needs to be small "seed" fractures called microfractures. Since microfractures can progress to macrofracture ("broken bone") or can be symptomatic in and of themselves ("stress fracture"), an imaging modality that is capable of displaying microfractures, or at least signatures of them, would be a great help to the bone mechanics research community. DEI is a new imaging modality that could potentially be capable of doing just that.

The existence and potential physiologic significance of microdamage accumulation in bone tissue has engendered considerable interest in the past 10 years. Part of the interest comes from the likely role of damage accumulation to the etiology of stress fractures [1,12,18-20,29] although some question it's role [23]. In addition, microdamage accumulation may contribute to osteoporotic fractures [4] and loosening of dental or orthopedic implants [16]. Microdamage, in addition to having a direct role on the degradation of bone mechanical properties [6,14,22], may contribute to clinical fractures and implant loosening by inducing bone remodeling, which under certain circumstances could lead to failure [18]. Some current treatments for osteoporosis work by inhibiting bone remodeling and there are now a number of reports that these treatments lead to accumulation of microdamage, sometimes with associated decrements in bone mechanical properties [13,27]. There is good evidence that microdamage accumulation increases with age [21,25], is associated with decreased mechanical properties [6,14,22] and initiates bone remodeling [2,3,5,24].

Current methods of identifying and characterizing microdamage in bone include stiffness loss in mechanical testing [7,8] as well as a number of microscopic techniques [11,15,17,26,28]. Here, we propose to determine if DEI has the potential to serve as a non-invasive way of directly identifying and characterizing microdamage in bone. The DEI method currently depends on a synchrotron as the source of x-rays, but in principle could be adapted to work with conventional x-ray sources.

DEI physics

Before beginning the discussion of DEI physics it is important to note that several papers have been written that relate the theory of DEI in far greater detail than will be presented here [9,10,30].

There are two essential physics principles that are used in DEI. The first is that light rays are refracted when they pass through an interface between two regions of different indices of refraction. Basically, what this means is that the light rays can deviate from their straight line path when they pass between areas of different densities. The second principle used is Bragg's Law, which is: $n\lambda = 2d\sin\theta$, where n is the order, λ is the wavelength, d is the lattice spacing of the crystal, and θ is the angle of incidence. This means that, for a given light energy, lattice spacing, and order, there is a very narrow range of angles of incidence for which reflection will occur. The narrow range of reflectivity is called the rocking curve, which has a peak at θ and has a full width at half maximum (FWHM) that is highly energy dependent, but usually on the order of a few microradians ($\sim 10^{-5}$ degrees).

The indices of refraction for x-rays passing through organic matter vary only slightly from the index of refraction of air. They are typically smaller than that of air by about one part in 10^6. This leads to angular deviations from a straight-line path that are on the order of tenths of microradians. These angular deviations cannot be measured in standard radiography, and actually result in a blurring effect in the image.

A third, important feature of DEI is its sensitivity to extinction. For example, extinction occurs commonly in fibrous materials. It results in radially symmetric ultra-small angle scattering (on the order of a couple microradians) in the sample.

Rocking curve

As previously stated, the analyzer crystal has a rocking curve which describes its angular intensity response. Placing an object in front of the x-ray beam before the analyzer crystal can result in a change in the measured rocking curve of the crystal. An object that only absorbs and refracts will cause the peak of the rocking

curve to be reduced and shifted though the width of the rocking curve will be unaffected. When the x-ray beam passes through the bone sample, the beam will experience some extinction effects due to the fibrous structure in the cortical bone. The extinction will result in a broadening of the rocking curve.

What was proposed for this experiment was that the introduction of microdamage into bone through fatigue loading would cause a further broadening of the rocking curve width. Microdamage would be expected to introduce additional surfaces in the interior of the bone. It was hypothesized that the cumulative effect of the x-ray beam passing through microdamage would be broadening of the rocking curve width.

Materials and methods

Though several different data sets were obtained, the general experimental procedure will be described here. The specific details for each data set are included in the previous sections.

Machined bovine cortical bone samples were prepared by the Rush group and shipped to the National Synchrotron Light Source (NSLS). The samples measured approximately 4mm by 4mm by 40mm. The samples were secured to an aluminum sample holder, to minimize movement during the imaging process, and then placed in a water-filled Lucite container. Image sets were obtained for each of the bone samples. The bones were then shipped to Rush where some bones were fatigue loaded, while the control bones were not fatigue loaded. After the bones were shipped back to the NSLS, image sets were again obtained for all of the bones.

A diagram of the experimental setup used to acquire all of the DEI and standard radiography data is included in Figure 1. All data were obtained at the NSLS Beamline X15A. White light entered the hutch through the beryllium window. Aluminum filters reduced the intensity of light entering the monochromator, removing most of the lower x-ray energies. The monochromator then selected out 40 KeV x-rays. An ion chamber then read the radiation dose to which the sample was exposed during imaging.

For each image set, a group of 101 images was obtained. The sample was positioned such that both the ambient (water only) and bone (bone surrounded by water) were in the field of view. The sample position remained fixed during all of the scans. Images were acquired for each analyzer crystal position as it was scanned from -10 to +10 μradians in 0.2 μradian steps. The shutter was closed for the last 5 images in order to determine the detector background. The exposure time for each image was 5 seconds. The detector that was used was a Rad-icon Shad-o-Box™ 2048 X-ray Camera which generates 2048 by 1024 images at 50 micron resolution.

The rocking curve widths were obtained using Interactive Data Language (IDL). The portion of the image that contained data (approximately 500 by 30 pixels) was cut out of the original image and the rest was discarded. The median for each individual step of the scan was found in the y-, or vertical, direction. For each value in the x-direction the median y value for each step was fit to a Gaussian and the full width at half of the maximum (FWHM) was found. The procedure was done both for the ambient and bone portion of each data set. Corrected rocking curve widths were calculated using equation one. $FWHM_{corrected} = \sqrt{(FWHM_{bone})^2 - (FWHM_{ambient})^2}$ **(equation 1)**

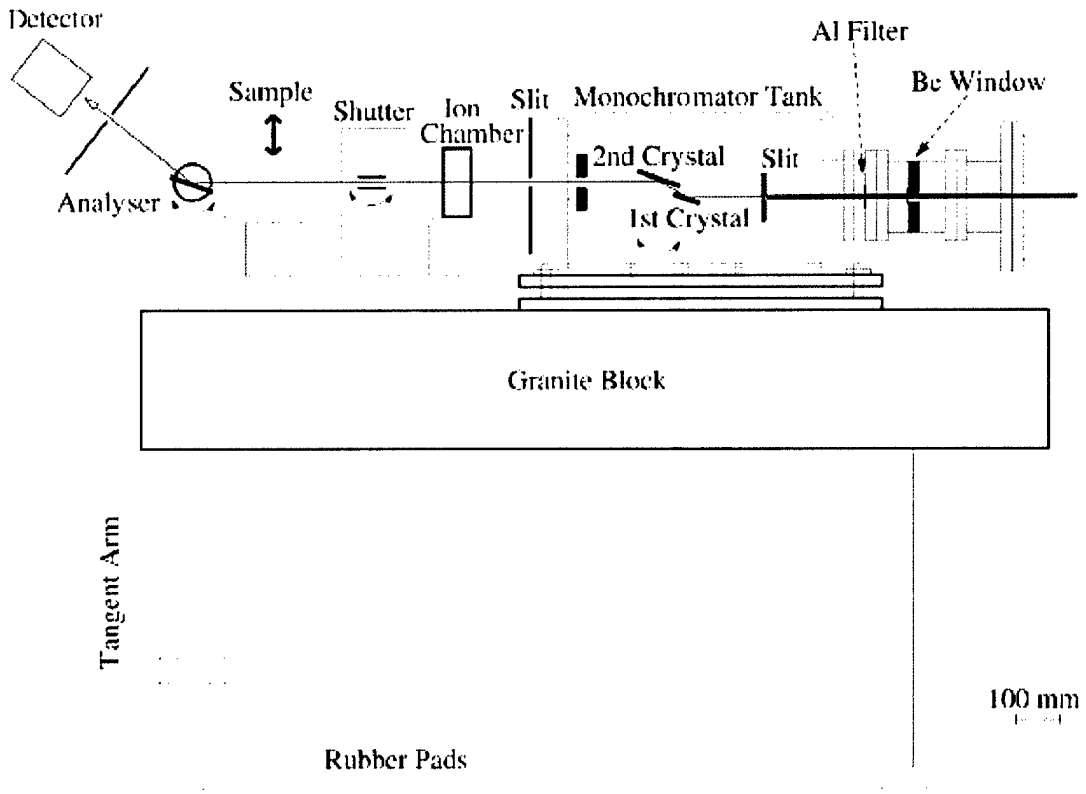

Figure 1- Experimental setup for Interface Gap and Drill Holes Experiments

Results and Discussion

A sample of a rocking curve fit with images at several points on the rocking curve is included in Figure 2. Note that, even though the sample bone had not yet been fatigue loaded, the rocking curve width of the bone is greater than the ambient rocking curve width. This broadening is expected because of extinction occurring in the bone. Note as well that there are clear structures (vascular channels) within the bone.

The data for all of the rocking curve widths obtained during the four separate experiments are shown in Table 1. Experiment 1 showed narrowing of the rocking curve in three of the four fatigued specimens from the first set of images (pre-fatigue loading) to the second set of images (post-fatigue loading) and narrowing in the control specimen from the first set of images to the second set of images. Experiment 2 showed an increase in the width of the rocking curve in all four fatigued specimens and the control specimen. Experiment 3 showed an increase in the width of the rocking curve in eight of nine fatigued specimens and the control specimen. Experiment 4 showed decreased rocking curve width in all eight fatigued specimens and all eight control specimens.

Even though all of the rocking curve widths tended to become narrower from image set 1 to image set 2 in Experiments 1 and 4, this narrowing was less in the specimens that were fatigued, suggesting that there was evidence of relative broadening of the rocking curve in the damaged specimens in these two experiments. However, in Experiments 2 and 3 the rocking curve width increased more in the controls than in the damaged specimens, suggesting that there was evidence of relative narrowing of the rocking curve in the damaged specimens in these two experiments. Thus, the data did not support the hypothesis that induction of fatigue damage would lead to broadening of the rocking curve width.

There are several factors that may have confounded the measured rocking curve widths. Drifting of the monochromator crystal, which is caused by temperature changes in the crystal, will cause a net broadening or narrowing effect on the rocking curve width. Calculating the corrected FWHM of the rocking curve was done to correct for this, but possibly did not fully correct the problem. A second factor that could have affected the results is

physical change in bone hydration due to water seeping either into or out of the bone. An experiment supporting this possibility was reported in the original final report (Experiments 1.2j-m). A third possibility is physical deterioration of the bone during the experiments, but this does not seem likely since they were stored in a 10% formalin solution when they were not being imaged.

Conclusions and future research

Overall, the rocking curve width experiments did not confirm the hypothesis. Several factors may have contributed in such a way as to make the results inconclusive. The experiments did have positive results in some respects. Images along the rocking curve clearly resolved objects of sizes that are within the resolving abilities of the detector. This suggests that, with a higher resolution detector, microfractures within the bone could be imaged. This experiment also led to a redesign of the monochromator. Temperature controls have been added which greatly reduce the amount of crystal drift within the monochromator.

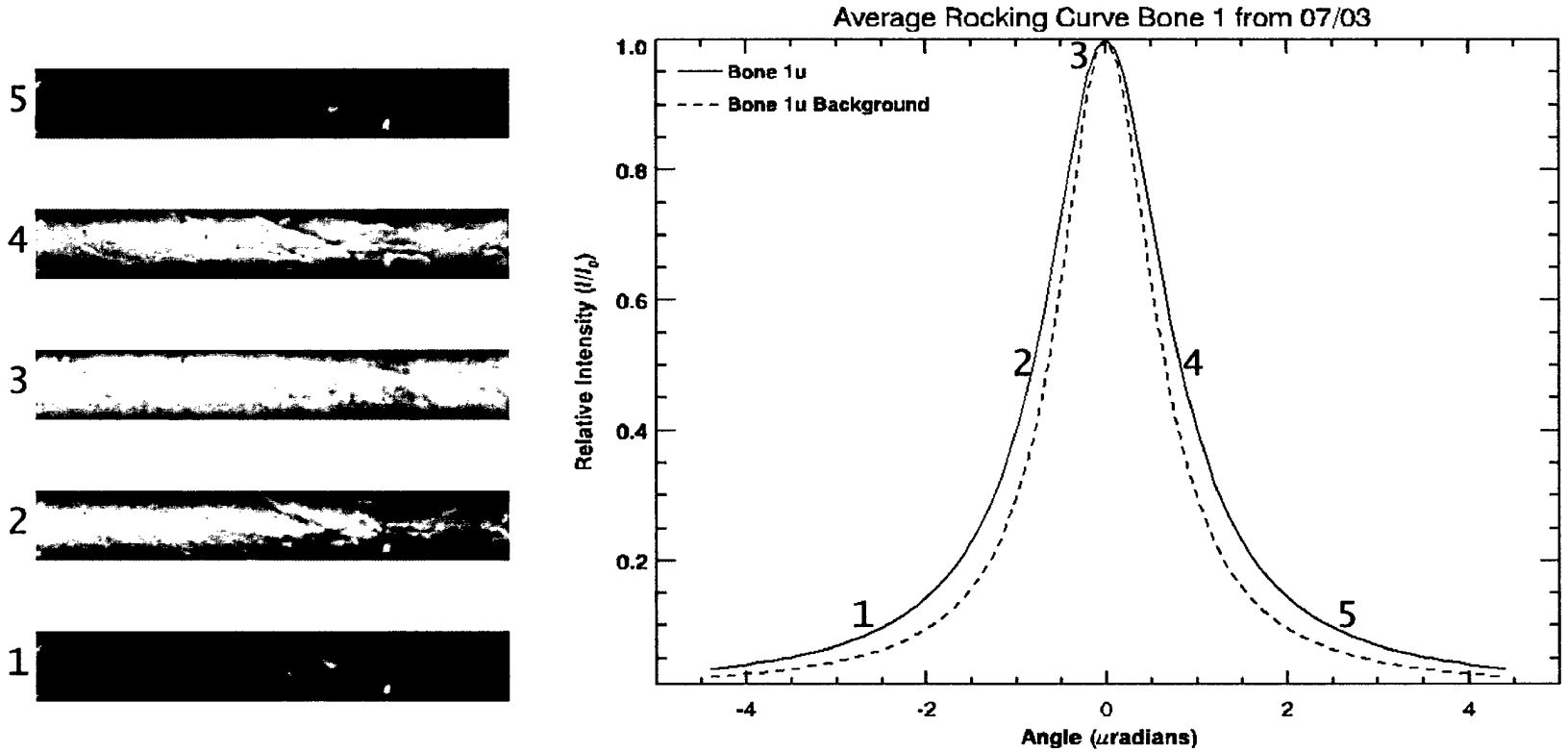

Figure 2- Example of rocking curves with accompanying images.

Combined Rocking Curve Data from All Pertinent Runs

Experiment	Sample	Tx	Pre-fatigue Ambient FWHM	+/-	Pre-fatigue Bone FWHM	+/-	Post-fatigue Ambient FWHM	+/-	Post-fatigue Bone FWHM	+/-	Pre-fatigue FWHM adjusted	+/-	Post-fatigue FWHM adjusted	+/-	Pre-Post FWHM adjusted	+/-
1	1	C	1.29	0.01	2.20	0.10	1.31	0.01	2.00	0.10	1.78	0.12	1.51	0.09	0.27	0.15
	2	F	1.31	0.01	2.10	0.20	1.31	0.01	2.00	0.10	1.64	0.26	1.51	0.09	0.13	0.27
	3	F	1.33	0.01	2.70	0.20	1.33	0.01	2.30	0.20	2.35	0.23	1.88	0.14	0.47	0.27
	4	F	1.31	0.01	2.30	0.40	1.34	0.01	2.40	0.10	1.89	0.49	1.99	0.07	-0.10	0.49
	5	F	1.33	0.01	2.20	0.20	1.28	0.01	2.00	0.10	1.75	0.25	1.54	0.08	0.22	0.26
		mean of Fatigued													0.18	
2	1	C	1.89	0.01	2.10	0.10	1.69	0.01	2.10	0.10	0.92	0.23	1.25	0.14	-0.33	0.27
	2	F	1.70	0.01	2.07	0.06	2.21	0.01	2.55	0.10	1.18	0.11	1.27	0.17	-0.09	0.20
	3	F	1.66	0.01	2.50	0.20	2.09	0.01	3.10	0.30	1.87	0.27	2.29	0.27	-0.42	0.38
	4	F	1.80	0.01	2.20	0.10	2.02	0.01	2.40	0.10	1.26	0.17	1.30	0.16	-0.03	0.23
	5	F	1.66	0.01	2.40	0.10	2.20	0.01	3.00	0.10	1.73	0.14	2.04	0.11	-0.31	0.18
		mean of Fatigued													-0.21	
3	1	C	1.28	0.02	2.14	0.08	1.27	0.01	2.61	0.18	1.71	0.10	2.28	0.21	-0.57	0.23
	2	F	1.23	0.02	1.48	0.08	1.27	0.01	1.61	0.05	0.82	0.15	0.99	0.08	-0.17	0.17
	3	F	1.23	0.02	2.21	0.11	1.30	0.01	2.76	0.16	1.84	0.13	2.43	0.18	-0.60	0.23
	4	F	1.31	0.02	1.66	0.05	1.33	0.02	1.79	0.06	1.02	0.09	1.20	0.09	-0.18	0.13
	5	F	1.24	0.02	1.49	0.05	1.33	0.01	1.62	0.05	0.83	0.10	0.92	0.09	-0.10	0.13
	6	F	1.24	0.03	1.80	0.17	1.34	0.01	1.94	0.18	1.30	0.24	1.40	0.25	-0.10	0.34
	7	F	1.25	0.02	1.78	0.16	1.31	0.01	1.99	0.12	1.27	0.23	1.50	0.16	-0.23	0.28
	8	F	1.24	0.02	1.71	0.07	1.31	0.01	1.79	0.06	1.18	0.10	1.22	0.09	-0.04	0.14
	9	F	1.23	0.02	1.58	0.06	1.31	0.01	1.72	0.05	0.99	0.10	1.11	0.08	-0.12	0.13
	10	F	1.23	0.02	1.96	0.13	1.33	0.02	1.97	0.09	1.53	0.17	1.45	0.12	0.07	0.21
		mean of Fatigued													-0.16	
4	1	C	1.27	0.01	1.46	0.03	1.32	0.01	1.46	0.03	0.73	0.06	0.61	0.07	0.12	0.09
	2	C	1.31	0.01	1.81	0.06	1.34	0.01	1.63	0.05	1.25	0.09	0.91	0.10	0.34	0.13
	3	C	1.31	0.01	1.60	0.04	1.34	0.01	1.55	0.04	0.92	0.07	0.78	0.09	0.14	0.11
	4	C	1.31	0.01	1.68	0.06	1.32	0.01	1.54	0.04	1.06	0.09	0.79	0.08	0.26	0.12
	5	C	1.42	0.01	2.03	0.09	1.44	0.01	1.84	0.06	1.45	0.13	1.15	0.09	0.30	0.16
	6	C	1.38	0.01	2.05	0.08	1.47	0.01	2.07	0.08	1.51	0.11	1.46	0.11	0.05	0.15
	7	C	1.39	0.01	1.66	0.03	1.49	0.01	1.70	0.03	0.91	0.06	0.81	0.06	0.10	0.08
	8	C	1.34	0.01	2.28	0.10	1.52	0.01	2.19	0.06	1.85	0.13	1.58	0.09	0.27	0.15
		mean of Control													0.20	
	9	F	1.30	0.01	1.64	0.05	1.33	0.01	1.62	0.04	1.00	0.08	0.91	0.07	0.08	0.11

Combined Rocking Curve Data from All Pertinent Runs																
Experiment	Sample	Tx	Pre-fatigue Ambient FWHM	+/-	Pre-fatigue Bone FWHM	+/-	Post-fatigue Ambient FWHM	+/-	Post-fatigue Bone FWHM	+/-	Pre-fatigue FWHM adjusted	+/-	Post-fatigue FWHM adjusted	+/-	Pre-Post FWHM adjusted	+/-
	10	F	1.23	0.01	1.51	0.04	1.34	0.01	1.54	0.03	0.88	0.08	0.75	0.06	0.12	0.10
	11	F	1.23	0.01	1.65	0.05	1.29	0.01	1.52	0.03	1.10	0.07	0.80	0.07	0.29	0.10
	12	F	1.18	0.01	1.70	0.06	1.30	0.01	1.63	0.06	1.22	0.08	0.98	0.10	0.24	0.13
	13	F	1.18	0.01	1.40	0.04	1.28	0.01	1.45	0.03	0.74	0.07	0.68	0.07	0.06	0.10
	14	F	1.02	0.01	1.52	0.09	1.31	0.01	1.69	0.08	1.13	0.12	1.07	0.13	0.06	0.18
	15	F	1.39	0.01	1.67	0.03	1.48	0.01	1.68	0.02	0.92	0.06	0.80	0.04	0.12	0.07
		mean of Fatigued													0.13	

Table 1- Summary of all rocking curve data

References

Reference List

1. Bennell KL, Malcolm SA, Wark JD, Brukner PD 1996 Models for the pathogenesis of stress fractures in athletes. [Review] [76 refs]. Br J Sports Med **30**:200-204.

2. Bentolila V, Boyce TM, Fyhrie DP, Drumb R, Skerry TM, Schaffler MB 1998 Intracortical remodeling in adult rat long bones after fatigue loading. Bone **23**:275-281.

3. Burr DB 1993 Remodeling and the repair of fatigue damage. [Review] [50 refs]. Calcif Tissue Int **53 Suppl 1**:S75-S80.

4. Burr DB, Forwood MR, Fyhrie DP, Martin RB, Schaffler MB, Turner CH 1997 Bone microdamage and skeletal fragility in osteoporotic and stress fractures. J Bone Miner Res **12**:6-15.

5. Burr DB, Martin RB, Schaffler MB, Radin EL 1985 Bone remodeling in response to in vivo fatigue microdamage. J Biomech **18**:189-200.

6. Burr DB, Turner CH, Naick P, Forwood MR, Ambrosius W, Hasan MS, Pidaparti R 1998 Does microdamage accumulation affect the mechanical properties of bone? [see comments]. J Biomech **31**:337-345.

7. Carter DR, Caler WE, Spengler DM, Frankel VH 1981 Fatigue behavior of adult cortical bone: the influence of mean strain and strain range. Acta Orthop Scand **52**:481-490.

8. Carter DR, Caler WE, Spengler DM, Frankel VH 1981 Uniaxial fatigue of human cortical bone. The influence of tissue physical characteristics. J Biomech **14**:461-470.

9. Chapman D, Thomlinson W, Johnston RE, Washburn D, Pisano, Gmur N, Zhong Z, Menk R, Arfelli F, Sayers D 1997 Diffraction enhanced x-ray imaging. Phys Med Biol **42**:2015-2025.

10. Dilmanian FA, Zhong Z, Ren B, Wu XY, Chapman LD, Orion, Thomlinson WC 2000 Computed tomography of x-ray index of refraction using the diffraction enhanced imaging method. Phys Med Biol **45**:933-946.

11. Fazzalari NL, Forwood MR, Manthey BA, Smith K, Kolesik P 1998 Three-dimensional confocal images of microdamage in cancellous bone. Bone **23**:373-378.

12. Frost HM 1998 A brief review for orthopedic surgeons: fatigue damage (microdamage) in bone (its determinants and clinical implications). [Review] [32 refs]. J Orthop Sci **3**:272-281.

13. Hirano T, Turner CH, Forwood MR, Johnston CC, Burr DB 2000 Does suppression of bone turnover impair mechanical properties by allowing microdamage accumulation? Bone **27**:13-20.

14. Hoshaw SJ, Cody DD, Saad AM, Fyhrie DP 1997 Decrease in canine proximal femoral ultimate strength and stiffness due to fatigue damage. J Biomech **30**:323-329.

15. Huja SS, Hasan MS, Pidaparti R, Turner CH, Garetto LP, Burr DB 1999 Development of a fluorescent light technique for evaluating microdamage in bone subjected to fatigue loading. J Biomech **32**:1243-1249.

16. Huja SS, Katona TR, Burr DB, Garetto LP, Roberts WE 1999 Microdamage adjacent to endosseous implants. Bone **25**:217-222.

17. Lee TC, Myers ER, Hayes WC 1998 Fluorescence-aided detection of microdamage in compact bone. Journal of Anatomy **193**:179-184.

18. Martin B 1995 Mathematical model for repair of fatigue damage and stress fracture in osteonal bone. J Orthop Res **13**:309-316.

19. Martin RB, Gibson VA, Stover SM, Gibeling JC, Griffin LV 1997 Residual strength of equine bone is not reduced by intense fatigue loading: implications for stress fracture. J Biomech **30**:109-114.

20. Muir P, Johnson KA, Ruaux-Mason CP 1999 In vivo matrix microdamage in a naturally occurring canine fatigue fracture. Bone **25**:571-576.

21. Norman TL, Wang Z 1997 Microdamage of human cortical bone: incidence and morphology in long bones. Bone **20**:375-379.

22. Norman TL, Yeni YN, Brown CU, Wang Z 1998 Influence of microdamage on fracture toughness of the human femur and tibia. Bone **23**:303-306.

23. Otter MW, Qin YX, Rubin CT, McLeod KJ 1999 Does bone perfusion/reperfusion initiate bone remodeling and the stress fracture syndrome? Medical Hypotheses **53**:363-368.

24. Parfitt AM 1993 Bone age, mineral density, and fatigue damage. [Review] [38 refs]. Calcif Tissue Int **53 Suppl 1**:S82-S85.

25. Schaffler MB, Choi K, Milgrom C 1995 Aging and matrix microdamage accumulation in human compact bone. Bone **17**:521-525.

26. Schaffler MB, Pitchford WC, Choi K, Riddle JM 1994 Examination of compact bone microdamage using back-scattered electron microscopy. Bone **15**:483-488.

27. Taylor M, Tanner KE 1997 Fatigue failure of cancellous bone: a possible cause of implant migration and loosening. [Review] [18 refs]. J Bone Joint Surg Br **79**:181-182.

28. Vashishth D, Koontz J, Qiu SJ, Lundin-Cannon D, Yeni YN, Schaffler MB, Fyhrie DP 2000 In vivo diffuse damage in human vertebral trabecular bone. Bone **26**:147-152.

29. Verborgt O, Gibson GJ, Schaffler MB 2000 Loss of osteocyte integrity in association with microdamage and bone remodeling after fatigue in vivo. J Bone Miner Res **15**:60-67.

30. Zhong Z, Thomlinson W, Chapman D, Sayers D 2000 Implementation of diffraction enhanced imaging experiments at the NSLS and APS. Nuclear Instruments and Methods in Physicis Research A **450**:556-567.

Diffraction Enhanced Imaging of Controlled Defects within Cortical Bone, Including Bone-Implant Interface Gaps

Statement of Problem

The purpose of this experiment was to compare images obtained using Diffraction Enhanced Imaging (DEI) with standard bone radiographs to determine which imaging modality is better able to resolve interface gaps and drill holes in bone.

Background

Interface gaps in bone implants

After bone implants are placed in bone it takes a period of time before the bone can completely heal around the implant. In addition, even after osseointegration has occurred, interface gaps can develop if there is net bone resorption at the interface as occurs in particle-induced osteolysis. The interface gap between the implant and the bone tissue can be very small (< 0.5mm). This size of interface gap is difficult to resolve with conventional radiography due to the narrowness of the interface region and the scattering that takes place in the bone. An alternative imaging modality would be helpful for visualizing interface gaps.

DEI physics

Before beginning the discussion of DEI physics it is important to note that several papers have been written that detail the theory of DEI in far greater detail than will be presented here [1,2,4].

There are two essential physics principles that are used in DEI. The first is that light rays are refracted when they pass through an interface between two regions of different indices of refraction. Basically, what this means is that the light rays can deviate from their straight line path when they pass between areas of different densities. The second principle used is Bragg's Law, which is: $n\lambda = 2d\sin\theta$, where n is the order, λ is the wavelength, d is the lattice spacing of the crystal, and θ is the angle of incidence. This means that, for a given light energy, lattice spacing, and order, there is a very narrow range of angles of incidence for which reflection will occur. The narrow range of reflectivity is called the rocking curve, which has a peak at θ and has a full width at half maximum (FWHM) that is highly energy dependent, but usually on the order of a few microradians (~10^{-5} degrees).

The indices of refraction for x-rays passing through organic matter vary only slightly from the index of refraction of air. They are typically smaller than that of air by about one part in 10^6. This leads to angular deviations from a straight-line path that are on the order of tenths of microradians. These angular deviations cannot be measured in standard radiography, and actually result in a blurring effect in the image.

In order to extract the refraction information in the sample, two images of the sample are obtained—one on the high-angle side of the rocking curve and another on the low-angle side. Two images can then be generated: the apparent absorption image and the refraction image. The apparent absorption image is essentially a scatter-reduced absorption image, so it should be similar in appearance to a standard planar radiograph. In planar imaging, the refraction image is just the total angular deviation of the beam as it passes through the sample—upward deflection is white, while downward deflection is black and zero deflection is mid-tone gray. The apparent absorption (I_r) and refraction ($\Delta\theta_z$) images are calculated using *equations 1* and *2* below.

$$I_r = \frac{I_H + I_L}{2} \quad \textbf{(equation 1)}$$

$$\Delta\theta_z = \frac{I_H R(\theta_L) - I_L R(\theta_H)}{R(\theta_L)\left.\frac{dR}{d\theta}\right|_{\theta=\theta_H} - R(\theta_H)\left.\frac{dR}{d\theta}\right|_{\theta=\theta_L}} \quad \textbf{(equation 2)}$$

DEI holds a lot of promise in the images of the interface gap region both because of its sensitivity to refraction and because of its scatter rejection properties.

Materials and methods

Two experiments were performed: (1) a drill hole experiment to determine if features within the resolving power of the detector could be better imaged with DEI than with conventional radiography and (2) an experiment to test the ability of DEI to resolve small bone-implant interface gaps (100 □m and 200 □m). For these experiments, two machined bovine cortical bone samples were prepared by the Rush group and shipped to the NSLS. The samples measured approximately 4mm by 4mm by 40mm. The sample for the drill hole experiment had four

parallel holes drilled perpendicular to the axial direction. The holes were separated by about 5 mm and measured 0.37mm, 0.5mm, 0.75mm, and 1mm in diameter. For the interface gap experiment, drill holes of radius 1mm were made through the center of the bone along the axial direction. Two titanium pins of the same radius were obtained. Each pin was 1.0 mm in diameter and approximately 15 mm long. For pin 1, 0.2mm was shaved off opposite sides of the rod along the length of the rod. For pin 2, 0.1mm was shaved off opposite sides of the rod along the length of the rod. The pins were then press fit into 1 mm diameter drill holes. Thus, pin 1 had 200 □m gaps along opposite faces of the bone-implant interface and pin 2 had 100 □m gaps. Two sets of images were obtained for each pin. In view 1, the x-ray beam was parallel to the shaved surfaces of the pin. In view 2 the specimen was rotated by 90° so that the x-ray beam was perpendicular to the shaved surfaces. Thus, in view 2, the gaps were in front of and behind the pin and in view 1 the gaps were adjacent to the pin.

A diagram of the experimental setup used to acquire all of the DEI and standard radiography data is shown in Figure 1. All data were obtained at the NSLS Beamline X15A. The samples were secured to an aluminum sample holder, to minimize movement during the imaging process, and then placed in a water-filled Lucite container. White light entered the hutch through the beryllium window. Aluminum filters reduced the intensity of light entering the monochromator, removing most of the lower x-ray energies. The monochromator then selected out 40 KeV x-rays. An ion chamber then read the radiation dose to which the sample was exposed during imaging.

For each image set, a subset of high angle, low angle and peak images were obtained. The high angle images were obtained by first finding the peak of the analyzer crystal and then rotating it by +0.8 μradians. Low angle images were obtained at -0.8 μradians from the peak. Background images (n=4) were obtained by keeping the shutter closed during the exposure time. The detector that was used was a Rad-icon Shad-o-Box™ 2048 X-ray Camera which generates 2048 by 1024 images at 50 micron resolution.

In order to do standard radiography scans, an image-plate (Fuji HRV) was placed on the sample stage. The same region was scanned through the beam as in the DEI configuration. The image-plate was scanned with a Fuji BAS2500 image-plate reader and saved.

Image reconstruction was done using Interactive Data Language (IDL). First, a median background image was created using the four background images. The background was then subtracted from each of the DE images. The refraction and apparent absorption images were then created using *equations 1* and *2*. The bone regions from all of the images were then cut out and comparison images were created.

Contrast to noise ratio (CNR) gains were computed by taking the ratio of the CNR for the DEI image to the CNR of the radiograph image [3]. Specifically, Contrast-to-noise ratio (CNR) is defined as: $CNR = \frac{I_{\max} - I_{bone}}{\sigma_{background}}$, where I_{bone} is the median of the section of bone surrounding the drill hole or interface gap and $\sigma_{background}$ is the standard deviation of an ambient section of the image. For the refraction images, the CNR is defined as:

$$CNR = \frac{\Delta\theta_{z,\max} - \Delta\theta_{z,\min}}{\sigma_{background}}.$$

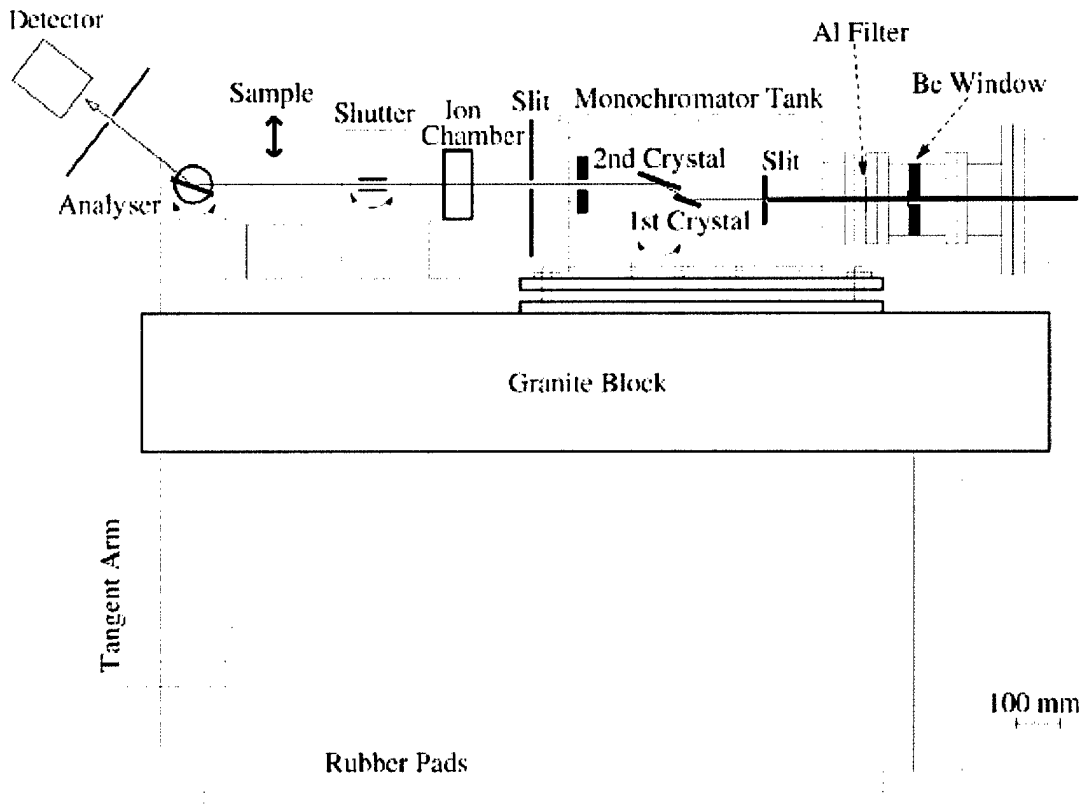

Figure 3- Experimental setup for Interface Gap and Drill Holes Experiments

Results and Discussion

A comparison of the radiograph, peak, apparent absorption, and refraction drill hole images is shown in Figure 2. A table of contrast-to-noise ratio (CNR) gains is included in Table 1.

All four drill holes can be seen in each image (Fig. 2). The refraction image clearly has the best drill hole contrast. Overall for the drill hole images, DEI images show large CNR gains over the radiograph images, an effect that is most evident for the smaller drill hole diameters with a CNR nearly 30-fold higher in the refraction image than in the radiographic image (Table 1).

For the interface gap experiment, comparisons of the radiograph, peak, apparent absorption, and refraction interface gap images are included in Figure 3. The gaps should appear in view 1 (x-ray beam parallel to the shaved surfaces), but for view 2 the gaps should be almost negligible (x-ray beam perpendicular to the shaved surfaces). Table 1 also displays the comparison of CNR gains across the interface gap.

As with the drill hole experiment, DEI shows substantial CNR gains when compared to the radiograph images. The interface gap region at the top and bottom edges of Pin #1 (200 □m gap) is barely visible in the radiograph, but appears very clearly in all three DEI images. The narrower interface gap surrounding Pin #2 (100 □m) cannot be seen in the radiograph image, but can be seen in all three DEI images and is most noticeable in the refraction image. The CNR gains for the DEI images confirm the visual observations (Table 1), where up to nearly 34-fold gains in CNR were found with the DEI images compared to standard radiography.

In all of the DEI images it should be noted that the refraction and apparent absorption components have not been completely separated. This can be most clearly seen in the bright and dark edges of the 0.50 mm drill hole in the apparent absorption image (Fig. 2). The apparent absorption should be a minimum at the center of the hole and should approach the apparent absorption of the bone at the edges of the hole. This effect is likely due to drifting in the monochromator crystals, which in turn led to the high- and low-angle images being taken asymmetrically about the peak of the rocking curve.

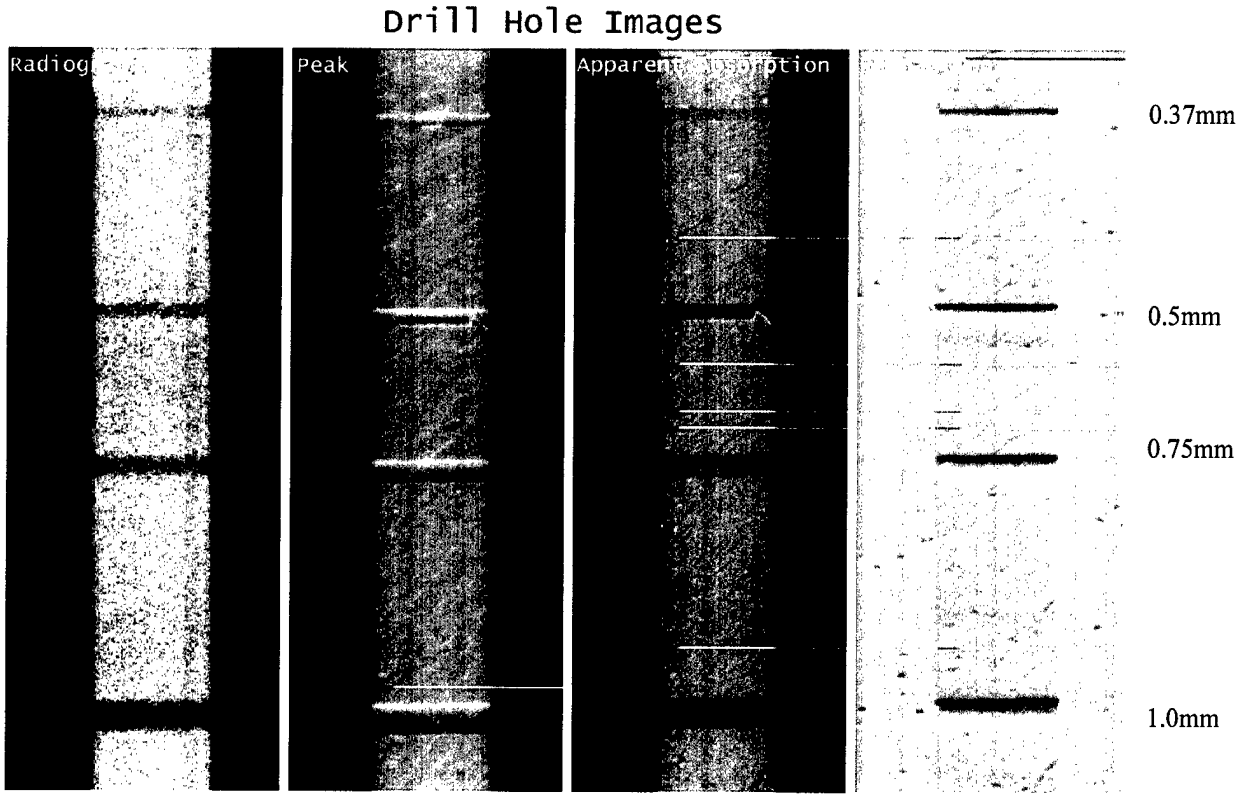

Figure 4- Drill hole image comparisons

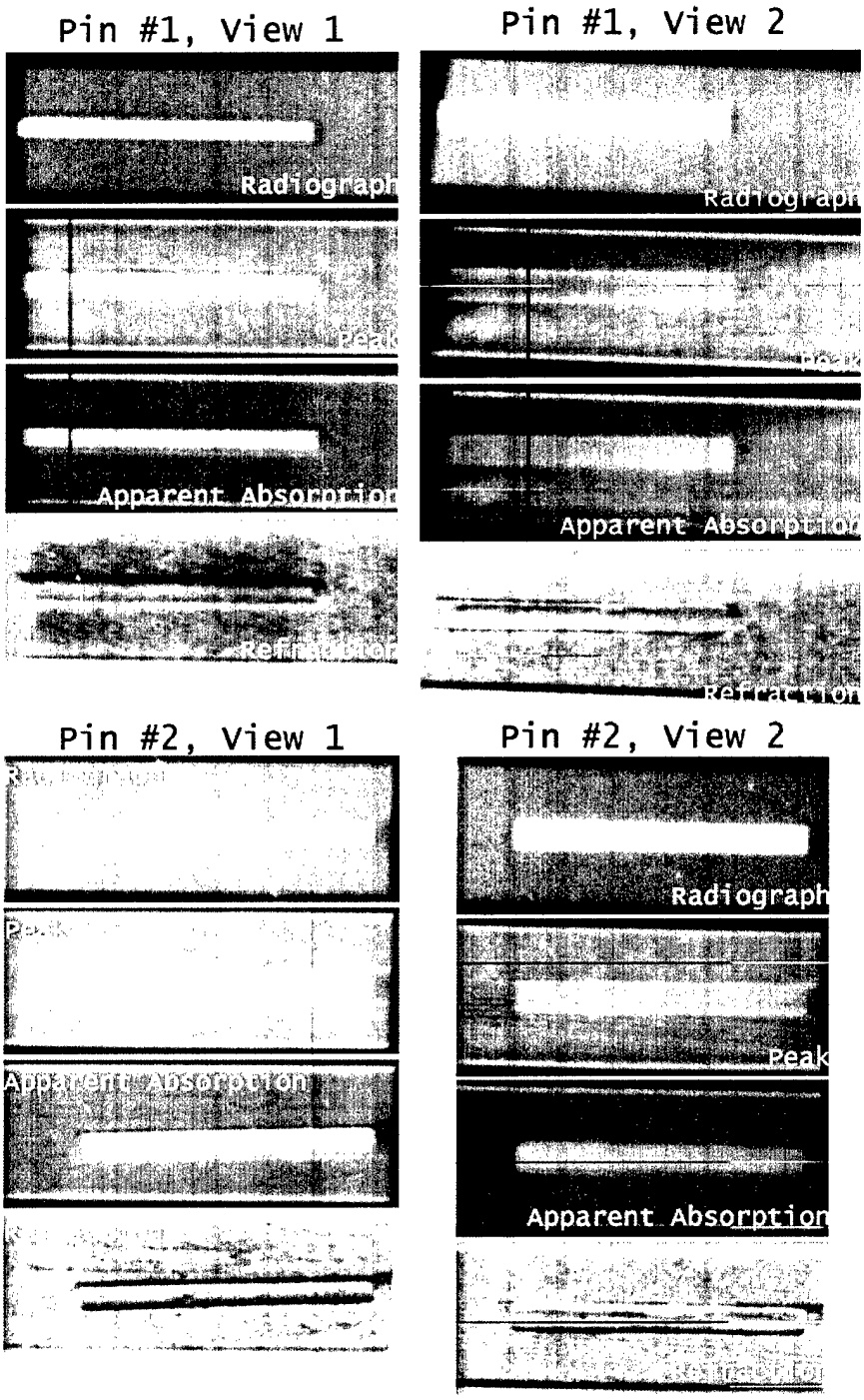

Figure 5- Interface gap comparison images. Note Pin #1 = 200 □m gap, Pin #2 = 100 □m gap. In View 1, the gaps are at the top and bottom edges of the pins. In View 2, the gaps are in front of and behind the pins. The 200 μm gaps are barely evident in the radiograph (Pin #1, View 1), but are clearly imaged in the DEI Refraction image (Pin #1, View 1). The 100 μm gaps are not evident in the radiograph (Pin #2, View 1), but are clearly evident in the DEI Refraction image (Pin #2, View 1).

Drill Hole Refraction Image CNR to Radiograph CNR ratio

Drill Hole Diameter (mm)	Ratio
0.37	29.8
0.50	19.9
0.75	14.8
1.00	12.0

Apparent Absorption Image CNR to Radiograph CNR ratio

Image	Ratio
Pin 1 View 1, top	7.6
Pin 1 View 1, bottom	3.7
Pin 2 View 1, top	6.0
Pin 2 View 1, bottom	4.0

Refraction Image CNR to Radiograph CNR ratio

Image	Ratio
Pin 1 View 1, top	8.7
Pin 1 View 1, bottom	5.6
Pin 2 View 1, top	19.4
Pin 2 View 1, bottom	33.7

Table 1-Comparison of DEI CNR gains

Conclusions and future research

These experiments are excellent tests of DEI because the structures being imaged were well within the resolving abilities of the detector. DEI showed CNR advantages over radiography in both experiments. It also showed the ability to resolve bone features that radiography could not resolve. This means that DEI has *both* contrast *and* resolution advantages over radiography for this set of images. Since there is usually a trade-off between resolution and contrast, this is a significant achievement.

Recent upgrades to the experimental equipment since work on the grant has ended have resulted in a significant reduction in the amount of drifting in the monochromator crystals, which should, in turn, lead to more consistent DEI images and a better separation of refraction and apparent absorption effects.

Reference List

1. Chapman D, Thomlinson W, Johnston RE, Washburn D, Pisano, Gmur N, Zhong Z, Menk R, Arfelli F, Sayers D 1997 Diffraction enhanced x-ray imaging. Phys Med Biol **42**:2015-2025.

2. Dilmanian FA, Zhong Z, Ren B, Wu XY, Chapman LD, Orion, Thomlinson WC 2000 Computed tomography of x-ray index of refraction using the diffraction enhanced imaging method. Phys Med Biol **45**:933-946.

3. Kiss MZ, Sayers DE, Zhong Z 2003 Measurement of image contrast using diffraction enhanced imaging. Phys Med Biol **48**:325-340.

4. Zhong Z, Thomlinson W, Chapman D, Sayers D 2000 Implementation of diffraction enhanced imaging experiments at the NSLS and APS. Nuclear Instruments and Methods in Physicis Research A **450**:556-567.

Three-dimensional Diffraction Enhanced Imaging

Statement of Problem

Diffraction Enhanced Imaging (DEI) shows contrast advantages over standard radiography in planar imaging. The goal of this experiment was to see if diffraction enhanced-computed tomography (DE-CT) also shows enhanced contrast when compared to standard x-ray CT.

Background

Trabecular bone

Osteoporosis is a metabolic disorder which is characterized by a decrease in bone density and a strength reduction in trabecular structure. Though osteoporosis damages both cortical and trabecular bone, its most detrimental effect is on the trabecular structure. Several different parameters have been established in order to characterize the trabecular bone strength. The most commonly measured parameter is the bone density, which is measured clinically using dual energy x-ray absorptiometry. Additional parameters can be measured using 3D imaging techniques. Some of the more common measurement parameters for 3D imaging are the ratio of bone volume to tissue volume, mean trabecular thickness, mean trabecular spacing, trabecular number, and trabecular connectivity. These parameters are not necessarily sufficient to completely describe the "bone quality" because bone strength is not always strongly correlated with these parameters. It would be helpful to develop measurements not dependent upon x-ray absorption in order to more completely describe the strength variation within the trabecular structure.

DEI physics

Before beginning the discussion of DEI physics it is important to note that several papers have been written that detail the theory of DEI in far greater detail than will be presented here [1-3].

There are two essential physics principles that are used in DEI. The first is that light rays are refracted when they pass through an interface between two regions of different indices of refraction. Basically, what this means is that the light rays can deviate from their straight line path when they pass between areas of different densities. The second principle used is Bragg's Law, which is: $n\lambda = 2d\sin\theta$, where n is the order, λ is the wavelength, d is the lattice spacing of the crystal, and θ is the angle of incidence. This means that, for a given light energy, lattice spacing, and order, there is a very narrow range of angles of incidence for which reflection will occur. The narrow range of reflectivity is called the rocking curve, which has a peak at θ and has a full width at half maximum (FWHM) that is highly energy dependent, but usually on the order of a few microradians (~10^{-5} degrees).

The indices of refraction for x-rays passing through organic matter vary only slightly from the index of refraction of air. They are typically smaller than that of air by about one part in 10^6. This leads to angular deviations from a straight-line path that are on the order of tenths of microradians. These angular deviations cannot be measured in standard radiography, and actually result in a blurring effect in the image.

In order to extract the refraction information in the sample, two images of the sample are obtained—one on the high-angle side of the rocking curve and another on the low-angle side. Two images can then be generated: the apparent absorption image and the refraction image. The apparent absorption image is essentially a scatter-reduced absorption image, so it should be similar in appearance to a standard planar radiograph. In planar imaging, the refraction image is just the total angular deviation of the beam as it passes through the sample—upward deflection is white, while downward deflection is black and zero deflection is mid-tone gray. The apparent absorption (I_r) and refraction ($\Delta\theta_z$) images are calculated using equations 1 and 2 below.

$$I_r = \frac{I_H + I_L}{2} \quad \textbf{(equation 1)}$$

$$\Delta\theta_z = \frac{I_H R(\theta_L) - I_L R(\theta_H)}{R(\theta_L)\left.\frac{dR}{d\theta}\right|_{\theta=\theta_H} - R(\theta_H)\left.\frac{dR}{d\theta}\right|_{\theta=\theta_L}} \quad \textbf{(equation 2)}$$

It has been shown that DE-CT is possible and can be computed using filtered-backprojection algorithms [1,2]. The refraction CT slices generated using DE-CT are a pixel-by-pixel representation of the out-of-plane gradient of the index of refraction. White pixels mean the gradient is positive, while black pixels mean negative. Mid-tone gray is the zero-refraction point. The refraction image is most sensitive to interfaces between different materials (i.e. brightest white/darkest black at bone/air interface), but it is also sensitive to out-of-plane density variations within the sample.

Materials and methods

The five trabecular bone samples of a range of bone volume per total volume values were received from Rush Medical College. Each bone was a cylinder measuring approximately 8 mm in diameter and approximately 1 cm long.

A diagram of the experimental setup used to acquire all of the DE-CT and standard CT data is included below (figure 1). All data were obtained at the National Synchrotron Light Source (NSLS) Beamline X15A. White light entered the hutch through the beryllium window. Aluminum filters reduced the intensity of light entering the monochromator, removing most of the lower x-ray energies. The monochromator then selected out 40 KeV x-rays. An ion chamber then read the radiation dose to which the sample was exposed during imaging. The sample was fixed to the top of a rotating stage.

For each image set, a subset of high angle, low angle and peak images were obtained. The high angle images were obtained by first finding the peak of the analyzer crystal and then rotating it by +0.8 μradians. Low angle images were obtained at -0.8 μradians from the peak. Each subset included 400 images. Of those, there were 20 white images, 20 dark images, and 360 images of the sample (taken in 1 degree rotational increments). The white images were obtained by lowering the sample until the x-ray beam no longer passed through it and then exposing the detector. The dark images were obtained by keeping the shutter closed during the exposure time. Exposure time for each of the 400 images was one second. The detector that was used was a Rad-icon Shad-o-Box™ 2048 X-ray Camera which generates 2048 by 1024 images at 50 micron resolution.

In order to do standard x-ray CT scans, the analyzer crystal was removed and the detector arm was rotated down in line with the beam. A set of 400 images was then obtained (as described above).

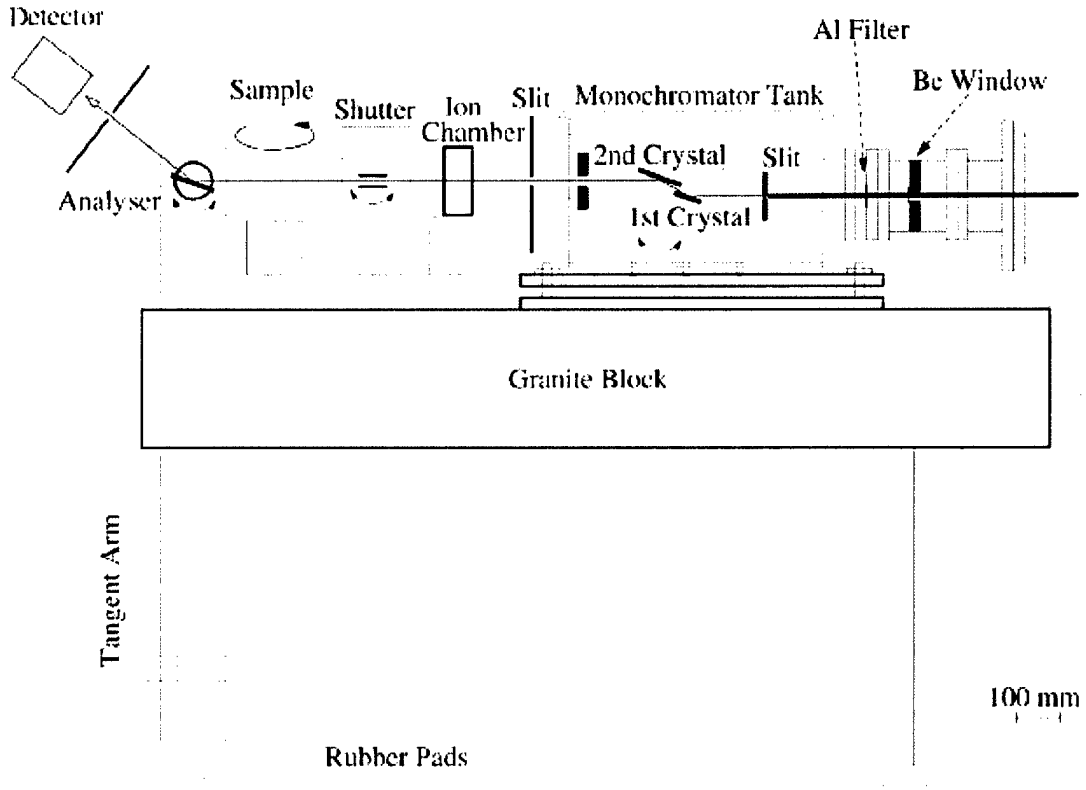

Figure 6- DE-CT experimental setup (Dilmanian, Zhong et al. 2000)

Since only a small portion of the detector was exposed the x-ray beam, that region of the image was saved, and the rest of the image was discarded. Computed tomography was then accomplished using IDL code developed by Mark Rivers (http://www-fp.mcs.anl.gov/xray-cmt/rivers/tutorial.html). A set of 33 apparent absorption, refraction, and standard x-ray CT slices were created for each bone sample.

Results and Discussion

A comparison of the apparent absorption, radiograph, and refraction slices is included in Figure 2.

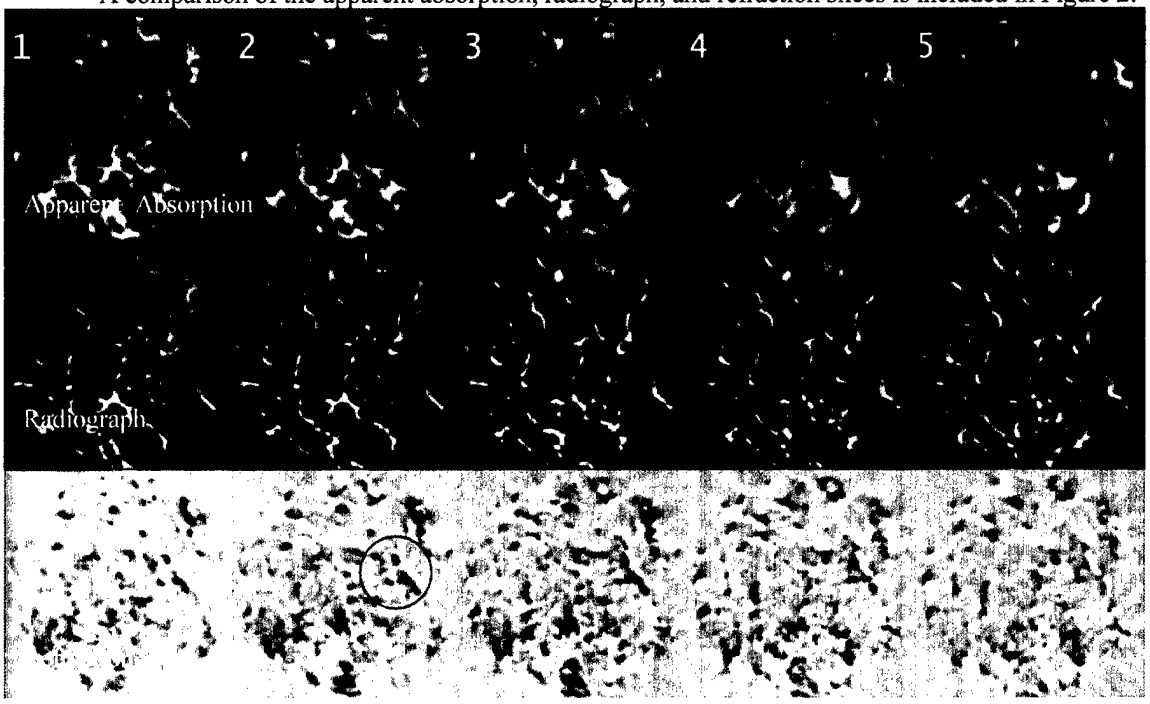

Figure 7- Apparent absorption, Radiograph and Refraction CT slices from Bone 2

It is clear from viewing the apparent absorption and radiograph CT slices that there is a consistency between the trabecular structure presented in each. The apparent absorption slice image shows the trabecular structure in more detail and more trabecular connectedness than that present in the standard x-ray CT slice as can be seen in the circled region. The additional detail is due to the scatter rejection inherent to the apparent absorption image. This increase in trabecular detail holds promise in that a higher resolution detector may be able to generate a 3D view of microfractures in bone.

It has been stated above that the refraction slice image is a representation of the out-of-plane gradient of the index of refraction. What results from this property is an edge-enhancement effect that is mostly clearly depicted in the circled region. Interfaces between the bone and the ambient air are either bright white or bright black. The refraction image is most sensitive to horizontal interfaces (e.g. air above bone), while it is not able to resolve vertical interfaces (e.g. vertical trabecular structure with air next to it).

Conclusions and future research

It has been shown here that high resolution DE-CT images of trabecular bone can be produced. These images show more detail as to the trabecular structure as compared to standard x-ray CT images obtained with the same imaging system. In addition to this, an additional image (refraction image) can be obtained that contains information not contained in the absorption image.

Further research needs to be performed in order to fully appreciate the significance of the refraction image. Questions about the best way to display the refraction information will need to be answered. Most importantly, the medical usefulness of the refraction image will need to be determined.

Reference List

1. Chapman D, Thomlinson W, Johnston RE, Washburn D, Pisano, Gmur N, Zhong Z, Menk R, Arfelli F, Sayers D 1997 Diffraction enhanced x-ray imaging. Phys Med Biol **42**:2015-2025.

2. Dilmanian FA, Zhong Z, Ren B, Wu XY, Chapman LD, Orion, Thomlinson WC 2000 Computed tomography of x-ray index of refraction using the diffraction enhanced imaging method. Phys Med Biol **45**:933-946.

3. Zhong Z, Thomlinson W, Chapman D, Sayers D 2000 Implementation of diffraction enhanced imaging experiments at the NSLS and APS. Nuclear Instruments and Methods in Physicis Research A **450**:556-567.